

Physical Optics and Electronics Group

1. Nanoscale Thermal Imaging of Semiconductor Devices

Research Staff

Dr. Dietrich Lürßen, Professor Janice A. Hudgings (Mount Holyoke College), Professor Rajeev Ram

Sponsors

DARPA: University Optocenters Program
NSF

Temperature profiling is of substantial interest in improving thermal design of thermoelectric, electronic and optoelectronic devices. We demonstrated previously the utility of thermal profiling using thermocouples as a non-invasive characterization method for various components of photonic integrated circuits, such as lasers [1] and absorbers [2]. By spatially profiling the heat exchange of a device with its environment, the optical distribution in the individual components, as well as a wide variety of intrinsic device parameters, can be precisely quantified over a wide range of operating conditions. While such studies are possible in principle using techniques such as spontaneous emission profiling, the advantage of thermal profiling is that the devices under study do not require any special processing, e.g., partial contact removal.

We have expanded these studies to analyzing gain saturation in semiconductor optical amplifiers (SOA) [3]. Using thermal profiling with thermocouples ($25 \times 25 \mu\text{m}^2$ footprint, 10mK resolution, 200mK accuracy), we were able to pinpoint the location of the onset of saturation experimentally (Figure 1). The experimental results agree quantitatively with theoretical modeling using spatially dependent rate equations (Figure 2). Thus, thermal profiling allows monitoring of the optical power profile inside optoelectronic devices under normal operating conditions. In order to extend this work to photonic integrated circuits, it is advantageous to have an imaging approach to thermal profiling rather than single point measurements as is the case when thermocouples are used.

As an all-optical method for measuring surface temperatures, thermorefectance is a useful approach. It relies on measuring the temperature-induced changes of the reflectivity of a gold- or semiconductor surface. We set up an experiment similar to the one described in [4], and found that we can achieve a temperature resolution of 25mK while having a spatial resolution of approximately 500nm (this is only limited by the optics currently in use, a 40x, NA=0.5 microscope objective, using light of 467nm wavelength). We achieved this extraordinary temperature resolution by matching the wavelength of light we used to a resonance of the contact material (gold). The experimentally determined temperature calibration coefficient $(\partial R/\partial T)/R = 3.29 \times 10^{-4} \text{ K}^{-1}$ is in perfect agreement with a calculation based on published material parameters of gold and the spectrum of the LED, and is about an order of magnitude larger than for white light or the HeNe laser wavelength. In Figure 3, thermorefectance measurements of surface cooling of a SOA due to optical amplification are shown. The surface temperature is lowered because in the amplification process, photons carry energy away. However, the device is not cooled in the process, it is only heated less.

In conclusion, spatially resolved thermal profiling is a powerful technique for wafer-scale, non-invasive mapping of the optical power distribution inside photonic integrated circuits. We have successfully demonstrated that the optical power distribution inside all active components of photonic integrated circuits (lasers, absorbers, amplifiers) can be successfully analyzed. We have further demonstrated that thermorefectance can yield a simultaneous measurement of many spatial points, making it ideal for the study of photonic integrated circuits.

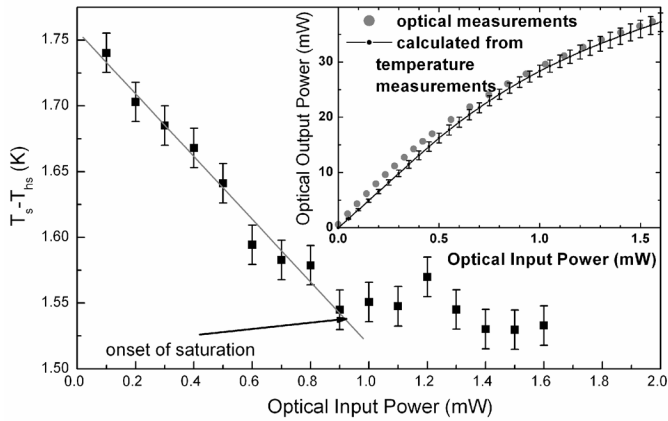


Fig. 1. Difference between the surface and heat sink temperatures at a fixed location ($z=1.45\text{mm}$) on the SOA as a function of the optical input power. Gain saturation becomes apparent at the point indicated by the arrow. The inset shows the comparison of measured and calculated optical output power of the SOA as a function of the input power.

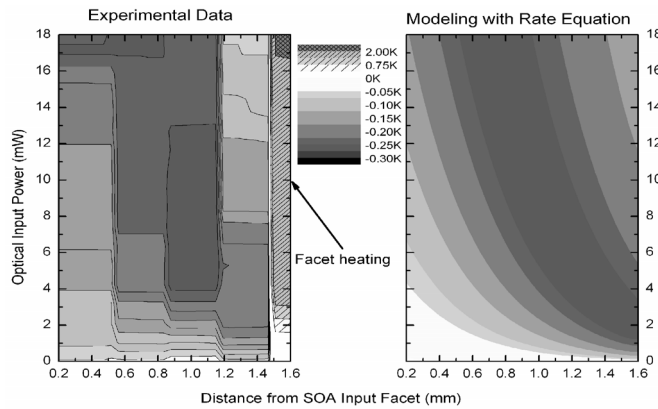


Fig. 2. Change in the SOA surface temperature (darker color represents more cooling) as a function of both the position on the SOA and the optical input power. The valley of maximum cooling (-0.3K) is seen in both experimental and calculated data. The least cooling is observed close to the input facet for small optical input powers.

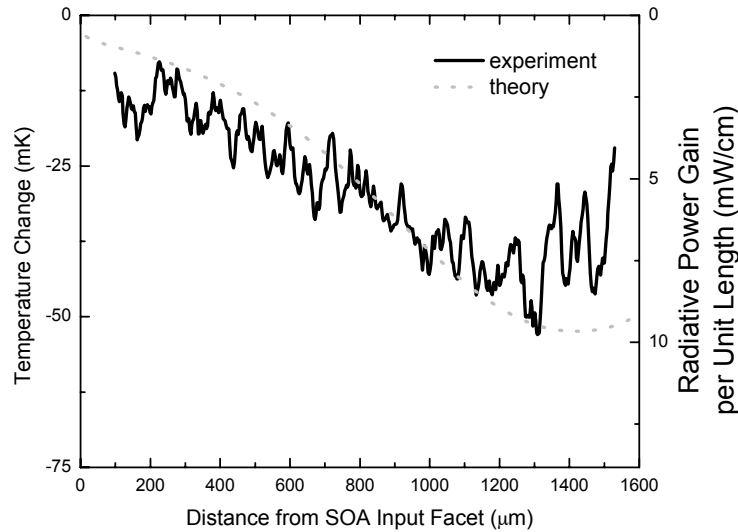


Figure 3. Surface temperature cooling (and corresponding optical power gain) along the length of the SOA due to optical amplification. For clarity, several adjacent data points have been averaged, leading to an effective spatial resolution of $\approx 15\mu\text{m}$. For comparison, modeling results using spatially dependent rate equations have been included in the plot.

References

1. K. P. Pipe and R. J. Ram, "Comprehensive Heat Exchange Model for a Semiconductor Laser Diode," *Photonics Technology Letters*, vol. 15, pp. 504-506, 2003.
2. J. A. Hudgings, K. P. Pipe, and R. J. Ram, "Thermal profiling for optical characterization of waveguide devices," *Applied Physics Letters*, vol. 83, pp. 3882-3884, 2003.
3. D. Lürßen, R. J. Ram, A. Hohl-AbiChedid, E. Clausen, and J. A. Hudgings, "Thermal Profiling: Locating the Onset of Gain Saturation in Semiconductor Optical Amplifiers," *Photonics Technology Letters, IEEE*, vol. 16, pp. 1625-1627, 2004.
4. S. Grauby, B. C. Forget, S. Hole, and D. Fournier, "High resolution photothermal imaging of high frequency phenomena using a visible charge coupled device camera associated with a multichannel lock-in scheme," *Review of Scientific Instruments*, vol. 70, pp. 3603-3608, 1999.

2. Waveguide Optical Isolators

Sponsor

DARPA: Air Force Research Laboratory

Project staff

Dr. Xiaoyun Guo, Tauhid Zaman, Professor Rajeev Ram

An optical isolator is a device that transmits light in only one direction. Optical isolators are required in optical communication systems to protect laser sources and optical gain elements. Available microoptic isolators are bulky and require expensive alignment. A waveguide isolator, which can be integrated with the source and other waveguide devices will be necessary for photonic integrated circuits.

A nonreciprocal polarization rotation is the key to an isolator's performance, i.e. coupling between TE and TM mode. Faraday rotation is a well-known nonreciprocal polarization rotation mechanism. The coupling ratio R is given by:

$$R = \frac{F^2}{F^2 + (\Delta\beta/2)^2},$$

where F is the Faraday constant and $\Delta\beta = \beta_{TE} - \beta_{TM}$ is the difference in the TE and TM propagation constants. We have observed Faraday rotation in doped InP with a Verdet coefficient of approximately $2.4^\circ/\text{mm}/\text{T}$ (Fig. 4) and a loss of 0.2cm^{-1} at 1550nm . The Verdet coefficient is the Faraday constant divided by the magnetic field intensity. In a waveguide with birefringence, the incomplete conversion of TE to TM and vice versa will confine the polarization rotation within a small angle. Thus a waveguide is required to have the same propagation constants for both TE and TM modes.

Birefringence arises from different sources including stress and waveguide geometry. We have developed techniques to fabricate birefringence free ridge waveguides. The waveguides consist of an InGaAsP core layer and InP cladding layers. Stress and photoelastic birefringence are negligibly small. To eliminate the shape birefringence, the ridge waveguide is designed to have a certain width and etching depth. In our process, high index contrast mesa is used. A 100nm Ti film is used as an etching mask. The ridge waveguide is etched using reactive ion etching with a mixture of hydrogen and methane. Fig. 5 is an SEM micrograph of the ridge waveguide and Fig. 6 shows the calculated geometric parameters for a birefringence free waveguide. The numerical simulation was performed using code developed by Mike Watts and Hermann Haus at MIT.

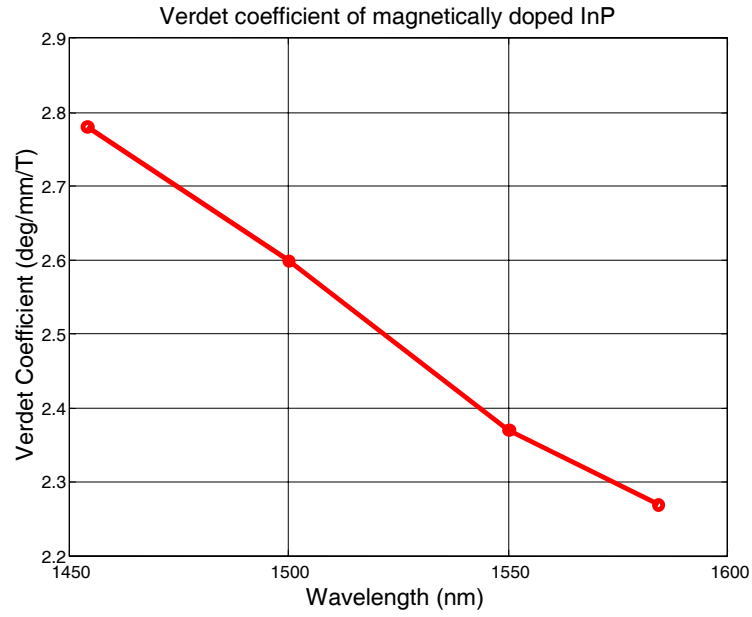


Fig. 4 Verdet coefficient of magnetically doped InP

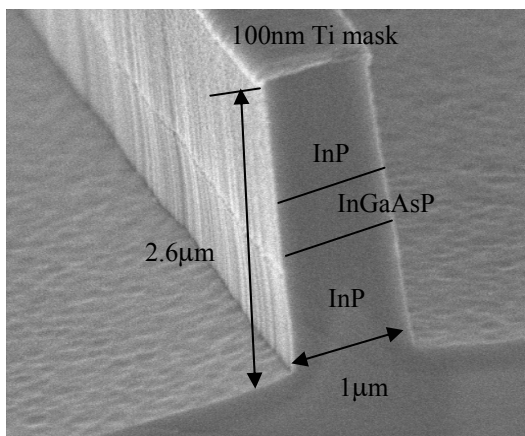


Fig. 5 SEM micrograph of a RIE etched ridge waveguide

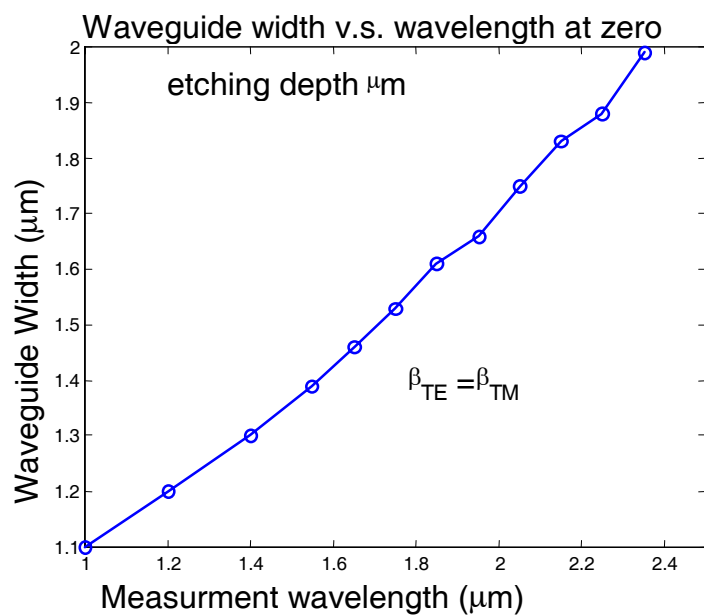


Fig. 6 Zero birefringence calculation for different waveguide widths and measuring wavelengths (2.5 μm etching depth for all waveguides)

3. Communications Technology Roadmap

Research Staff

Elizabeth Bruce, Professor Rajeev J. Ram

Sponsor

Microphotonics Center Industry Consortium

The MIT Communications Technology Roadmapping (CTR) program is focused on roadmapping integrated photonics. The project is unique in that it incorporates a deep understanding of the underlying photonic technologies with a comprehensive view of the communications value chain, including industry, business, and policy dynamics. Roadmapping can serve as a powerful tool for academia, business and government by creating a framework to think about future technology development and to help focus technology development efforts and guide allocation of resources and investment.

The CTR program incorporates two key methodologies for roadmapping: 1.) analytical modeling tools and 2.) industry-based working groups.

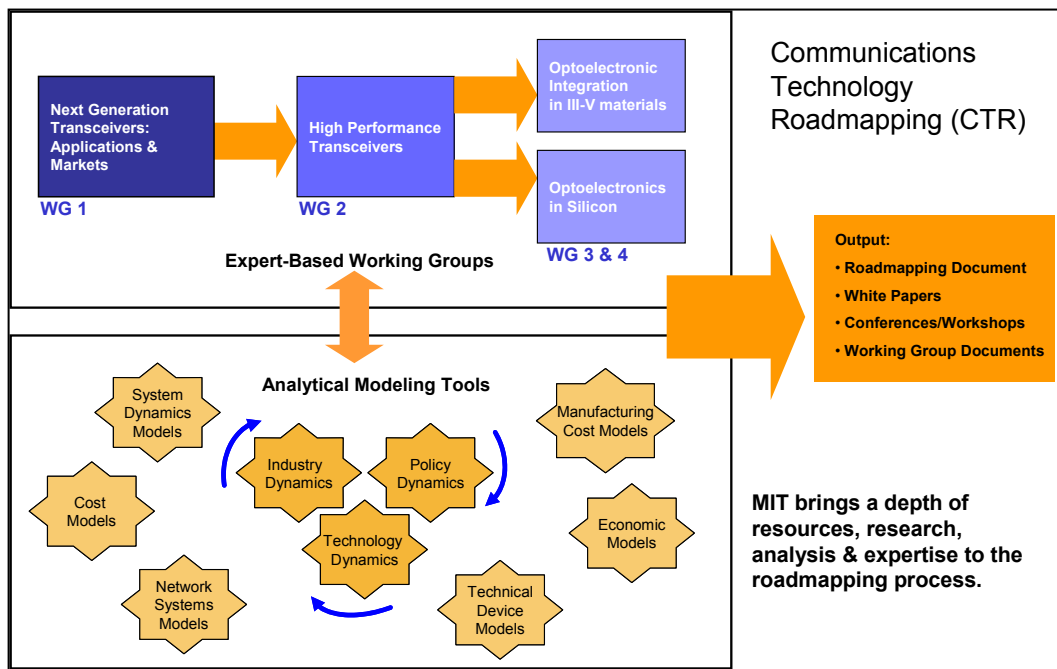


Fig. 7 Communications Technology Roadmapping methodologies.

Analytical modeling tools provide us with a means of analyzing the many complex factors that shape this industry and the advancement of related technologies. CTR is developing a set of predictive models including physical device models, process-based cost models, economic models, and system dynamics models - all of which will contribute to the roadmapping process and provide us with a means for investigating future scenarios.

Since 2002, CTR has conducted a series of Working Groups (WG). These WGs bring together leading industry experts from across a broad range of disciplines contributing to the design, manufacture, and application of optoelectronic components. Working Group members provide expert testimony, as well as contribute valuable information to the CTR models and analysis. We currently have four on-going WGs (see Fig. 8)

<p>WG 1: “Next Generation Transceivers: Applications, Markets, and Economics” (NGT WG) The NGT WG will assess future market drivers and demand for optical transceivers and identify potential opportunities to drive convergence across multiple applications and segments of the industry.</p>
<p>WG 2: “High Performance Transceivers” (HPT WG) The HPT WG will focus on roadmapping optical transceivers for communications applications. This group will identify the different functional requirements and will examine how they might effectively be integrated.</p>
<p>WG 3: “Silicon Opto-Electronic Devices” (Silicon WG) The Silicon OE WG will discuss the development of key functions in silicon (e.g. sources; detectors; modulators) and will examine the critical barriers. Discussions will include: optical I/O; material augmentation (including SiGe, BaTiO3); and manufacturing silicon photonic devices using foundry services.</p>
<p>WG 4: “Opto-Electronic Integration in III-V Materials” (III-V WG) The goal of the III-V WG is to examine the major barriers for integration of various electronic and optical functions in III-V materials. This WG will study the critical manufacturing processes that govern yields for III-V devices.</p>

Fig. 8 Communications Technology Roadmap working groups.

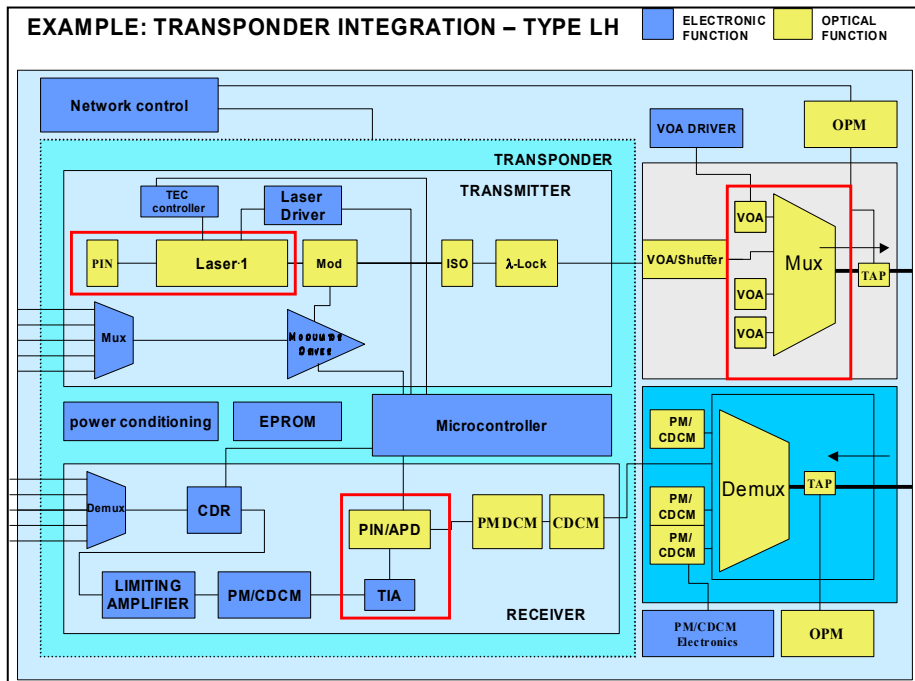


Fig. 9 shows the basic opto-electronic functions incorporated in a DWDM optical networking transponder – the key functional building blocks for integration.

In addition to the Working Groups, the Communications Technology Roadmap program includes a range of in-depth modeling projects involving both Engineering and Sloan school students. More information on the project is available at <http://mph-roadmap.mit.edu>.

4. Warm Electron Transport Dynamics in a 2DEG

Research Staff

M.C. Abraham (RLE and Harvard Physics), Prof. Rajeev J. Ram (EECS)

Sponsor

National Science Foundation

In this project we study the temperature dependence of the individual momentum scattering processes in modern high mobility AlGaAs/GaAs 2DEG heterostructures (HM2DEGs). For a bulk semiconductor, the “equilibrium” mobility, μ (i.e. when the electron temperature $T_e = T_L$ the lattice temperature), first rises and then falls as a function of temperature T . Reduction in impurity scattering as electrons become more energetic causes the initial rise, and the onset of phonon scattering triggers the eventual fall. By contrast, in HM2DEGs, μ falls monotonically as a function of T as shown in Fig. 10 (black solid line). Most of the donor impurities in these structures are spatially separated from the transport channel, and therefore impurity scattering is greatly reduced and dominates only at very low temperatures. All further reduction in μ is attributed to the onset of phonon scattering. This simple monotonic temperature dependence of μ in a HM2DEG masks the temperature dependence of the individual scattering processes.

The transport properties of HM2DEGs have been extensively studied in the last few decades [1-3]. Most experiments and theory have focused on either quantum or many-body effects at low temperature or at higher temperatures for electronics where optical phonon scattering and intersubband scattering dominate. We have made theoretical calculations in the regime of “warm” electrons where the electronic temperature is greater than the lattice temperature $T_e > T_L$ (T_L fixed at 1K and T_e ranging from 1K to 40K). In this regime the temperature dependence of the individual momentum scattering processes emerge clearly.

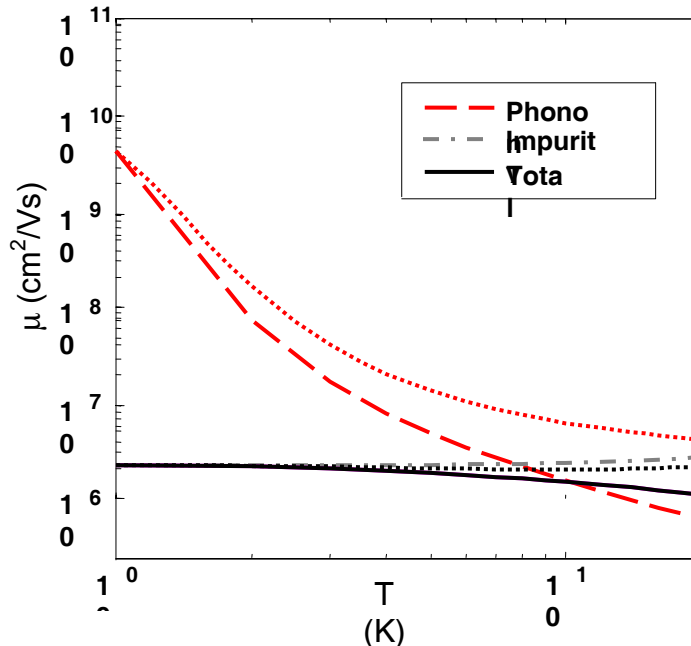


Fig. 10: The two components that contribute to the total mobility in a typical HM2DEG are plotted. The labels “ph” and “imp” correspond to phonon and impurity limited scattering respectively. Total mobility is drawn with the solid black line and is labeled “all”. Impurity scattering depends only on T_e . Dotted lines are plots for “warm” electrons, i.e. the mobility calculations where T_L is fixed at 1K and only the T_e is varied. Impurity scattering depends only on T_e . The electron density is chosen to be $n = 2.7 \times 10^{11} / \text{cm}^2$ and μ at $T = 0$, is set to $2.3 \times 10^6 \text{ cm}^2 / \text{Vs}$. The B-G transition temperature is $T_{BG} \approx 8\text{K}$.

An illustration of transport regimes that are clearly observed in warm electron HM2DEG's is the Bloch-Grüneisen (BG) phenomena. The BG regime refers to the temperature range in which phase space restrictions prevent electrons from emitting phonons with sufficient momentum so as to cause large angle scattering. The critical temperature at which this effect occurs is given by $T_{BG} \approx 2k_f \hbar s / 2\pi k_B$, where k_f is the Fermi wavelength, \hbar the Plank constant, s the speed of sound, and, k_B the Boltzman constant. For temperatures below T_{BG} , phonon scattering has a T^{-5} dependence. Since the mobility is dominated by remote impurity scattering below T_{BG} for most HM2DEG samples the temperature dependence of acoustic phonon scattering that is the hallmark of Bloch-Grüneisen (BG) phenomena can be $\sim 10^{3-4}$ smaller than the temperature independent part (impurity scattering); this small BG signature was measured indirectly by Stomer *et al* [4]. In Fig. 10, the relative contributions of the phonon and impurity scattering are plotted in the case of "equilibrium" (solid lines) and "warm" (dashed lines) electrons.

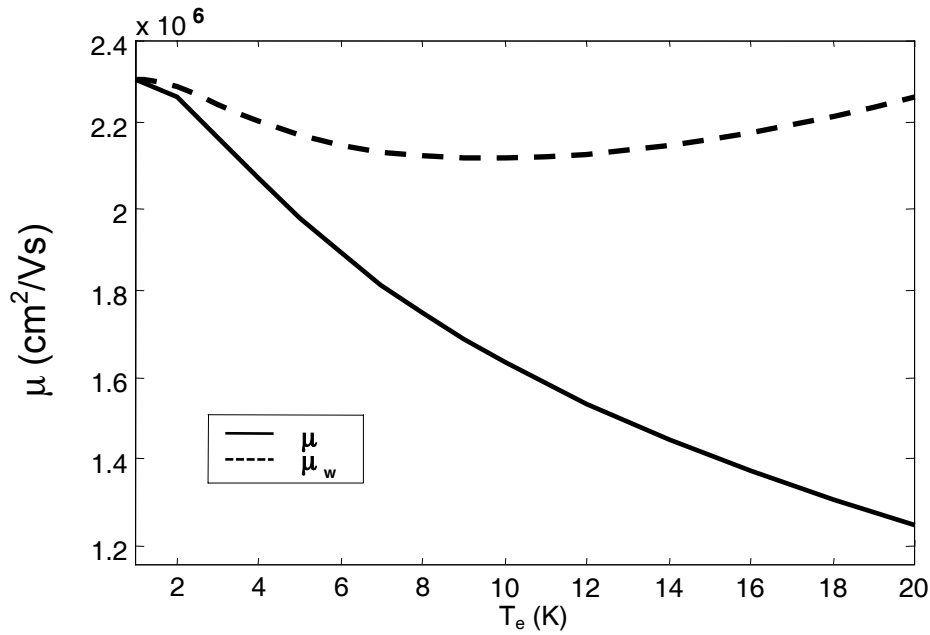


Fig. 11. μ and μ_w from Figure 1, plotted on a linear scale. For μ_w , T_L is fixed at 1K. The initial dip in μ_w is caused by the B-G phenomena and the eventual rise by the reduction in impurity scattering.

Our theory shows that for HM2DEG's with low temperature mobilities greater than $200\text{m}^2/\text{Vs}$ and electron densities of $\approx 2 \times 10^{15}/\text{m}^2$, the mobility as a function of T_e (with T_L fixed at 1K) can fall by as much as 5-10% till $T_e \approx T_{BG}$, and then rise as a result of reduced impurity scattering. In Fig. 11 both the total "equilibrium" mobility μ and the "warm" electron mobility μ_w is shown on a linear scale. The dip in the mobility as T_e rises, occurs as a result of the competition between the T^{-5} escalation of phonon scattering caused by the BG effect (hence the initial fall in mobility) and subsequent reduction of impurity scattering (resulting in the eventual rise). These results illustrate transport effects due to the BG phenomena that are two orders of magnitude larger than what has previously been studied by Stomer *et al* [4].

References

- [1] T. Ando, A.B. Fowler, and F. Stern, Rev. Mod. Phys., **54**, 437 (1982)
- [2] B. Huckestein, Rev. Mod. Phys. **67**, 357 (1995)
- [3] H. L. Stomer, D. C. Tsui, and A. C. Gossard, Rev. Mod. Phys. **71**, S298 (1999)
- [2] H.L. Stomer, L. N. Pfeiffer, K.W. Baldwin, and K.W. West, Phys. Rev. B, **41**, 1278 (1990)

5. Absorption Linewidth of CdSe/ZnS Nanocrystals

Research Staff:

Tom Liptay, Rajeev Ram
Brent Fisher, Mounji Bawendi

Sponsor:

Packard Foundation

Researchers have proposed using semiconductor nanocrystals (NCs) in a wide variety of applications including quantum information processing, biological imaging, data storage, and optical devices. The motivation for this research comes primarily from the potential application of NCs for quantum information processing (QIP). An important parameter in determining the usefulness of NCs for QIP applications is the dephasing rate of excitons in NCs. (Dephasing is caused by phonon scattering, surface scattering, and population decay.) An upper bound on the dephasing rate is set by the absorption linewidth of the NCs.

We plan to use a pump-probe setup to measure the absorption linewidth of a CdSe/ZnS capped NC sample. The basic idea is that a pump laser excites excitons in the CdSe/ZnS NCs, thus changing the transmission through the sample (since there are less NCs in the ground state to absorb light). An AOM modulates the pump beam power, which in turn modulates the transmission through the sample. This change in transmission is measured using a lock-in amplifier to detect the modulation in the transmitted probe laser. Using a similar experimental setup, researchers have measured a 1.5 GHz absorption linewidth in CdSe/ZnS capped NCs. [1]

As a preliminary experiment, we have measured the absorption lifetime of the NCs at room temperature in solution (toluene). We did this by using a pump laser to modulate the transmission of the NC sample, while probing the transmission with probe laser at the same wavelength. (Fig. 12) Using a lock-in amplifier we measured the phase lag of the probe beam with respect to the phase of the pump beam. We then plotted the phase lag vs. modulation frequency and fit the data to a single exponential decay. The result is a 20 ns absorption lifetime. (Fig. 13) Additionally, we measured the radiative lifetime of the dots by exciting them with a green LED and measuring the phase lag of the NC fluorescence. The measured 28 ns radiative lifetime agrees with the 25 ns lifetime measured using a time domain technique on the same sample by Brent Fisher.

Next, we plan to put the dots in a polymer and repeat the lifetime measurements in the polymer as a function of temperature.

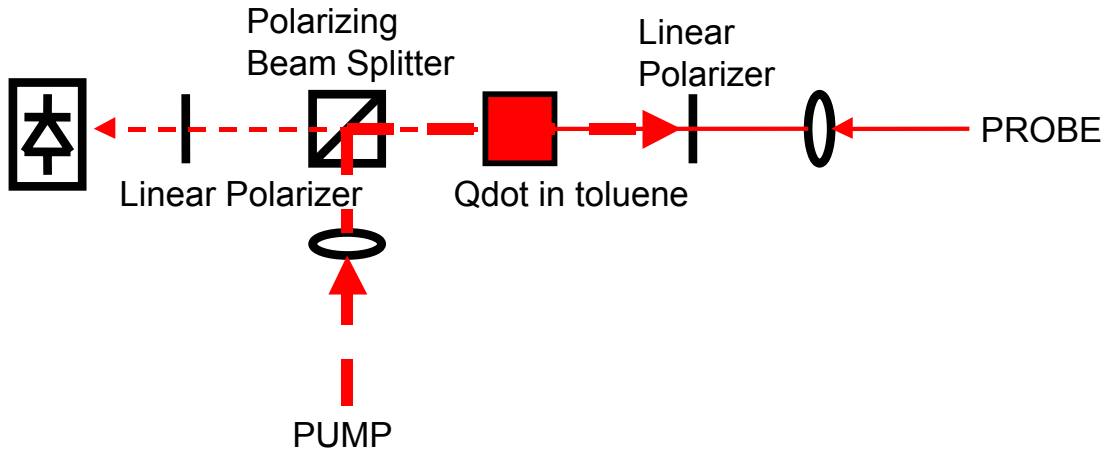


Figure 12: A pump laser is used to modulate the transmission of the NC sample. The resulting modulation of the transmitted probe laser is measured using a lock-in amplifier. The sample (provided by QDot Corp) has an absorption peak at 650 nm. The lasers are 5 mw diode lasers at 635 nm.

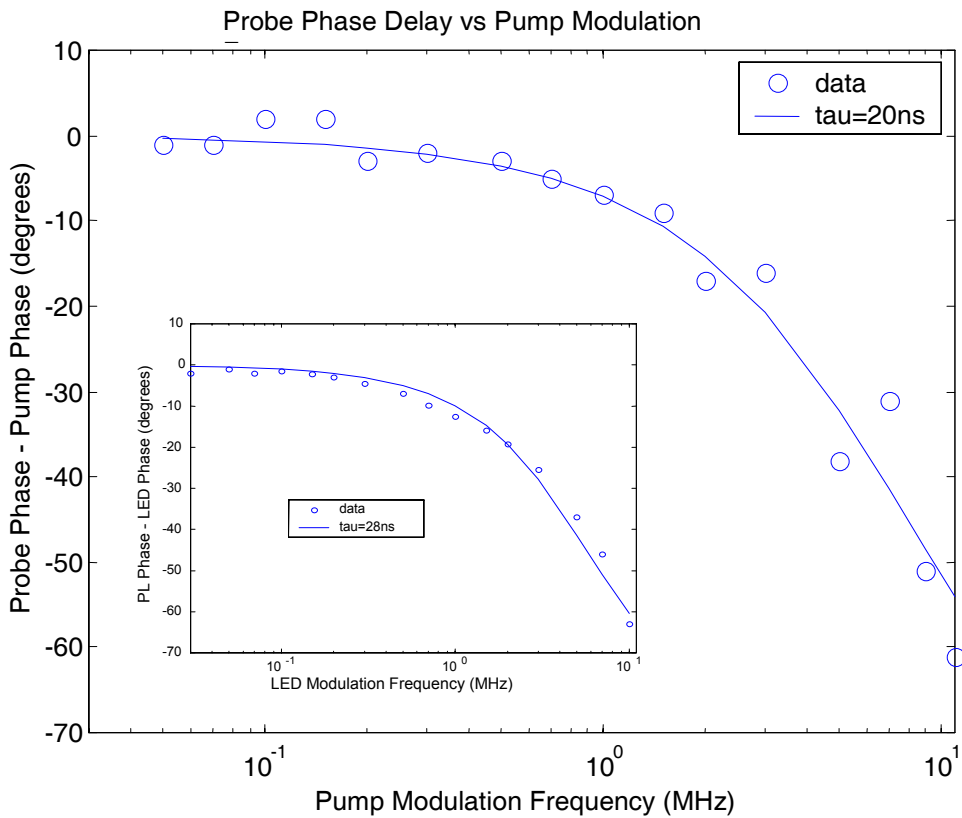


Figure 13: The phase delay of the probe with respect to the pump laser is measured using a lock-in amplifier. The dashed line shows a 20 ns single exponential fit to the data. Inset: A green LED is used to excite the sample. The phase delay of the fluorescence is plotted vs LED modulation frequency and fit to a 28 ns single exponential.

6. Direct Thermal to Electrical Energy Conversion

Research Staff:

P. M. Mayer, R. J. Ram

Sponsor:

ONR (MURI)

This project is directed towards the development of a thermoelectric generator (TEG) to be used for the recovery of energy from hot bodies in the temperature range 300-650 degrees Celsius. A TEG relies on the transport of charge carriers in a material hot on one side and cold on the other to drive an electrical current through a load, generating useful electrical power from heat (Seebeck/Peltier effects). Efficiency and power density are the two most common measures of TEG system performance, while the traditional metric quantifying the effectiveness of a material for a TEG is the thermoelectric figure of merit Z . Ideally, the Z of the material and the temperatures of the hot and cold sides of the generator are sufficient to characterize the maximum efficiency of the generator. The output power density of the generator can then be set independently by scaling the geometry of the TE material. Maximum power output is then obtained by matching the load resistance of the generator to the total internal resistance of the TE material. As a result, considerable effort has been spent in the thermoelectric community trying to improve the Z of thermoelectric materials.

When a more realistic model of a thermoelectric generating system is considered, the simple picture breaks down. The changes from the ideal model are particularly apparent for thin devices with large power fluxes, for which ideal constant temperature boundary conditions are unphysical. In this case, we have found that the operation of the device is constrained by a heat-sink's ability to maintain the temperature difference across the generator. Recent advances in thin-film thermoelectric materials [1, 2] promise to increase the generated power density significantly, at the price of increased stress on the heat sink.

Simulations show that in heat-sink limited conditions the simple figure of merit is no longer sufficient to characterize the generator efficiency (Fig. 14) and the load matching condition does not necessarily maximize power (Fig. 15). The results promise to provide a better picture of what determines the performance of a real thermoelectric generator, and suggest directions for future system improvement.

[1] R. Venkatasubramanian, E. Silvola, T. Colpitts, and B. O'Quinn, *Nature* **413**, 597 (2001)

[2] T. C. Harman, P. J. Taylor, M. P. Walsh, and B. E. LaForge, *Science* **297**, 2229 (2002)

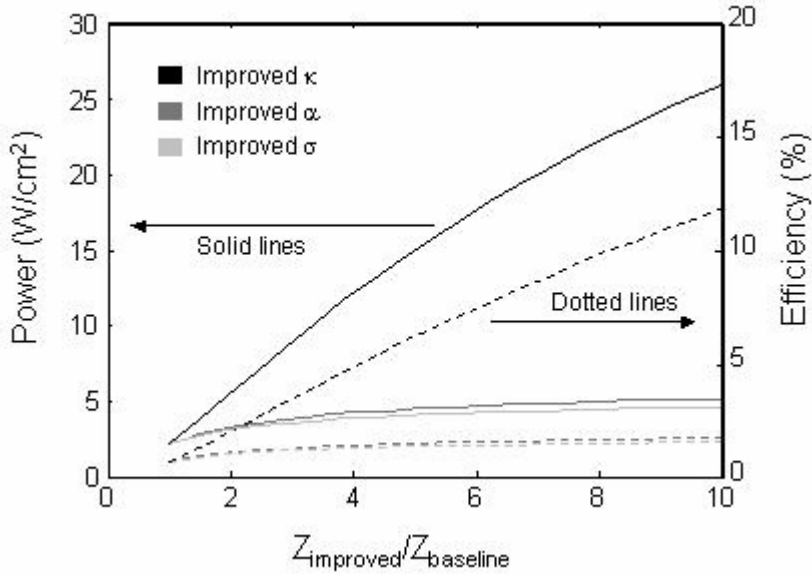


Fig. 14 Generated power and efficiency for improvements in thermal conductivity (κ), Seebeck coefficient (α), and electrical conductivity (σ) under heat-sink limited conditions.

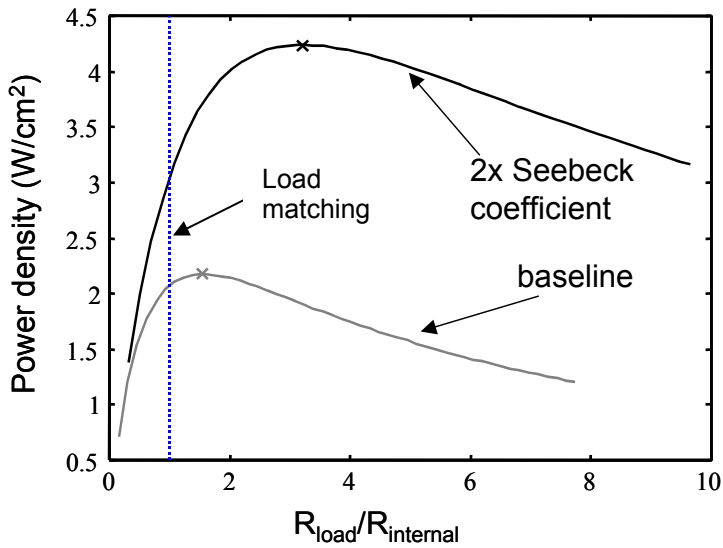


Fig. 15 Power density as a function of load resistance for a baseline material (SiGe) and a material of enhanced Seebeck coefficient. Note that in both cases, the optimal load resistance is larger than the (traditionally assumed) load matching condition.

7. Optical Sensing of Bioprocesses

Research Staff

Harry Lee, Professor Rajeev J. Ram
Paolo Boccazzi, Professor Anthony J. Sinskey
Professor Klavs Jensen

Sponsor

DuPont MIT Alliance

An ideal bioprocess monitoring tool would be able to analyze all components in bioprocess media with high sensitivity *in-situ*, which would eliminate errors due to physiological disturbance during sampling, reduce contamination risk, and allow higher measurement frequency. As a non-invasive optical technique, Raman spectroscopy has the potential for approaching this ideal tool. However, to realize this potential will require developing a method to achieve reliable concentration estimations from Raman spectra collected through scattering media with widely varying optical density, and quantifying sensitivity limits and sources of error. To resolve these issues, we are focusing on explicit least squares methods, which do not require a lengthy calibration process and can tolerate the widely varying optical densities encountered during fermentations.

Previously, we had shown the feasibility of using Raman spectra to estimate the composition of bacteria growth culture from samples taken from a *Corynebacterium* bioreaction. In this update, we demonstrate concentration estimation from *in-situ* measured Raman spectra. Fig. 17 shows the experimental setup used to measure Raman spectra *in-situ* from a 2.5L stirred tank bioreactor. A commercial Raman probe (InPhotonics) was adapted to allow sterile interfacing to a 19mm standard port. Raman spectra were collected at approximately 30 minute intervals using a total 5 minute integration time, broken into thirty, 10 second intervals. Concentration estimates were obtained by least squares fitting to measured pure spectra and internally referencing the concentrations to the extracted contribution from water. Results are shown in Fig. 18. The errors were primarily caused by systematic modeling errors, rather than any signal to noise limitation. Shot-noise limited detection limits are predicted to be on the order of 0.1mM, indicating significant improvements are possible.

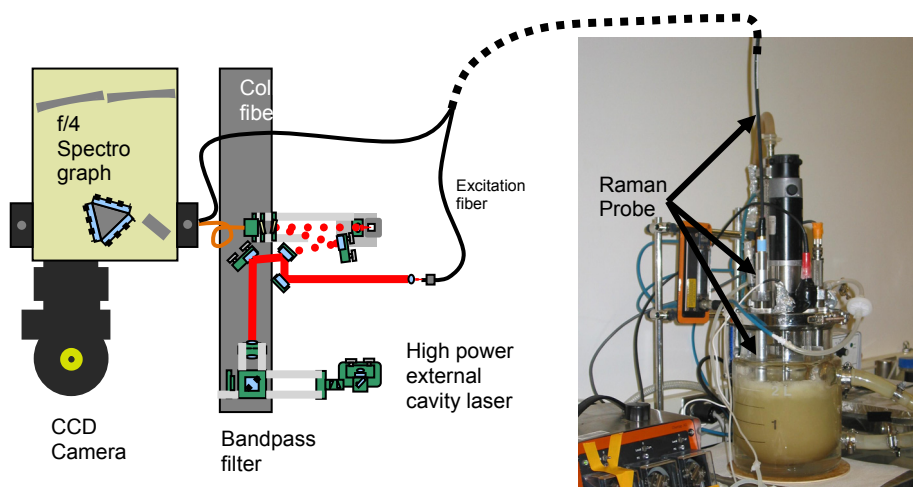


Fig. 17 Experimental setup for *in-situ* Raman spectra measurement. A commercial Raman probe was adapted to interface to a standard 19mm port of a 2.5L stirred tank bioreactor.

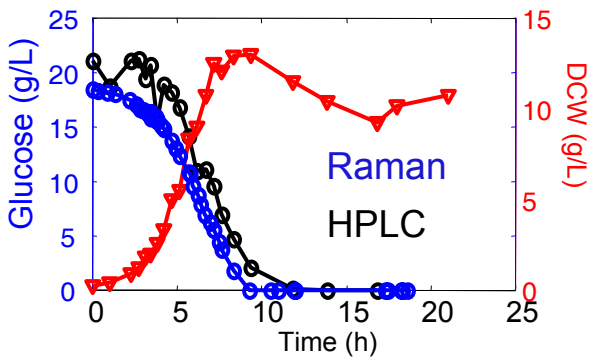
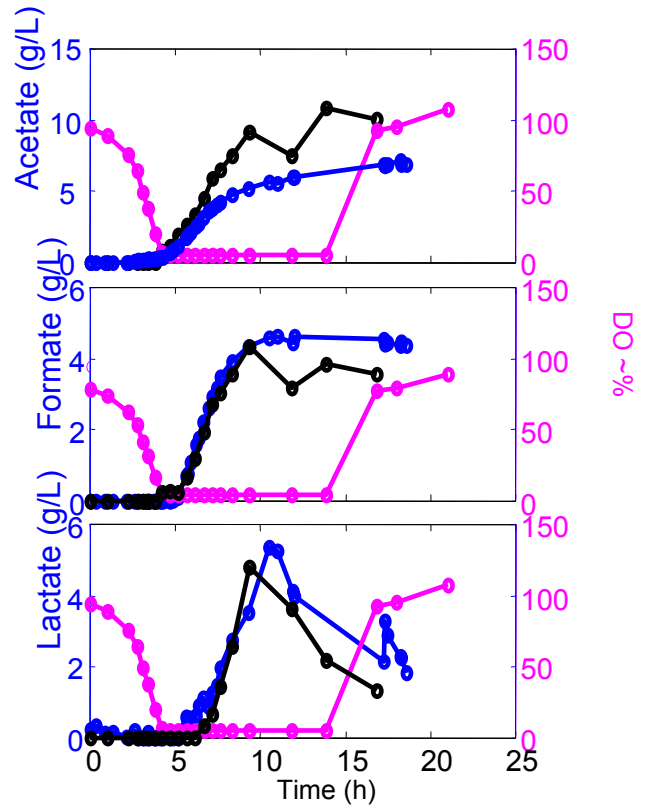


Fig. 18. Comparison of concentration estimates from in-situ measured Raman spectra and HPLC reference measurements for glucose, acetate, formate, and lactate. Raman spectra were measured in-situ from a phenylalanine *E. coli* (ATCC 31883) growth on defined medium.



References

- [1] Harry L. T. Lee, Paolo Boccazzi, Nathalie Gorret, Rajeev J. Ram and Anthony J. Sinskey, "In situ bioprocess monitoring of *Escherichia coli* bioreactions using Raman spectroscopy", *Vibrational Spectroscopy*, Vol. 35, Issues 1-2, 17 June 2004, pp 131-137.

8. Parallel Integrated Bioreactor Array

Research Staff

Harry Lee, Professor Rajeev J. Ram
Paolo Boccazzi, Professor Anthony J. Sinskey
Professor Klavs Jensen

Sponsor

DuPont MIT Alliance

We are developing a system to perform multiple microbial growth experiments in parallel with the aim of facilitating bioprocess development and fundamental studies of the dynamic response of microbes to changing conditions. Key attributes for such a system are the ability to provide high oxygen transport rates to support aerobic growth to high cell density; in-situ measurement of culture parameters; ease of use, setup and maintenance; and scalability to large numbers of reactors. These attributes motivate a miniaturized solution and the design of meso-scale fluidic devices.

One such device is the peristaltic oxygenating mixer, which combines mixing capability, critical for ensuring culture homogeneity and pH control, and oxygenation to support aerobic growth. It is composed of a flat enclosed volume where the top wall is composed of a thin membrane with 7 separate actuatable areas, as shown in Fig. 19. By pressurizing the actuatable areas in sequence, peristalsis can be approximated, driving a transverse fluid flow, which provides homogeneous mixing in approximately 10 seconds. This can be compared to the diffusion time which is on the order of 10 hours. This mixing device is easily scalable since the peristaltic mixing tubes can be shared by many wells. Current prototypes share mixing tubes among four wells. Fig. 20 shows snapshots of a 150 μ L volume mixer as mixing progresses. Residual inhomogeneity is due to non-uniform lighting.

Initial bacteria growth experiments have been carried out in the peristaltic oxygenating mixer, with integrated oxygen sensors and optical density measurements in four growth wells. Fig. 21 shows growth curves and dissolved oxygen measurements for four simultaneously run bioreactions of a phenylalanine producing *E. coli* strain, using defined medium with and without MES buffer. Until approximately 6 hours into the growth, the oxygen concentration was manually controlled to stay above 75% by adjusting the peristalsis period. The oxygenation rate was reduced briefly at approximately 11 hours and turned off at 16 hours to establish the deoxygenated baseline. The growth curves for the two medium compositions correspond well with each other and relatively high optical densities of 7.4 and 9.3 were reached with and without buffering.

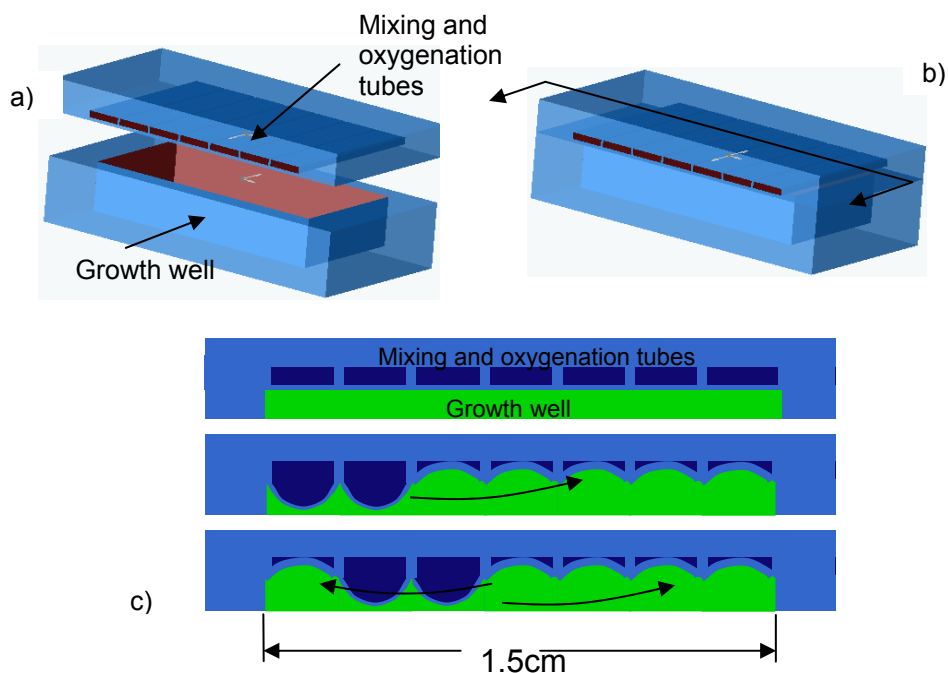


Figure 19 a) Exploded view of a single peristaltic oxygenating mixer. b) Peristaltic oxygenating mixer, cross section plane indicated. c) Cross section view showing peristalsis and actuation. The mixing and oxygenation tubes are actuated by air pressure, which deflects the membrane at the bottom of the tube to approximate peristalsis.

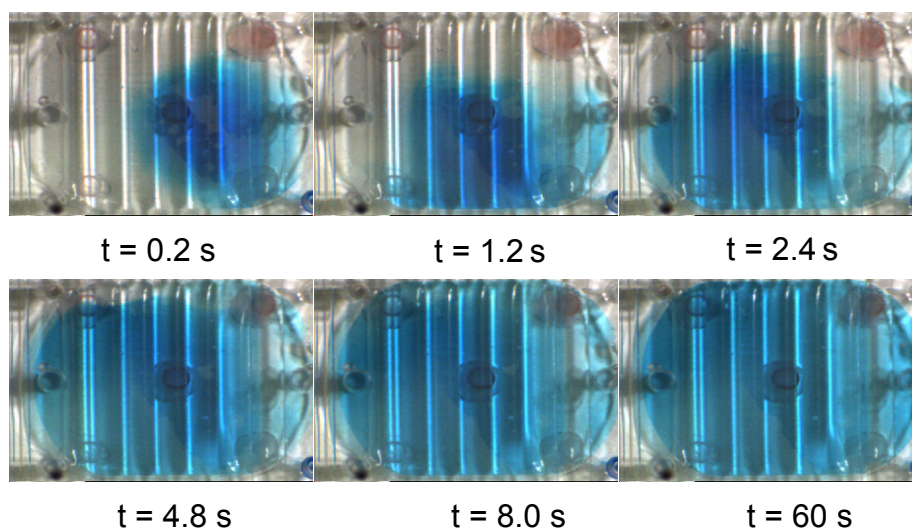


Fig. 20 Snapshots of mixing for a 0.2 second peristalsis period. 6psi actuation pressure. Complete mixing in approximately 10 seconds. Residual inhomogeneity is due to non-uniform lighting and reflections and refraction from internal interfaces.

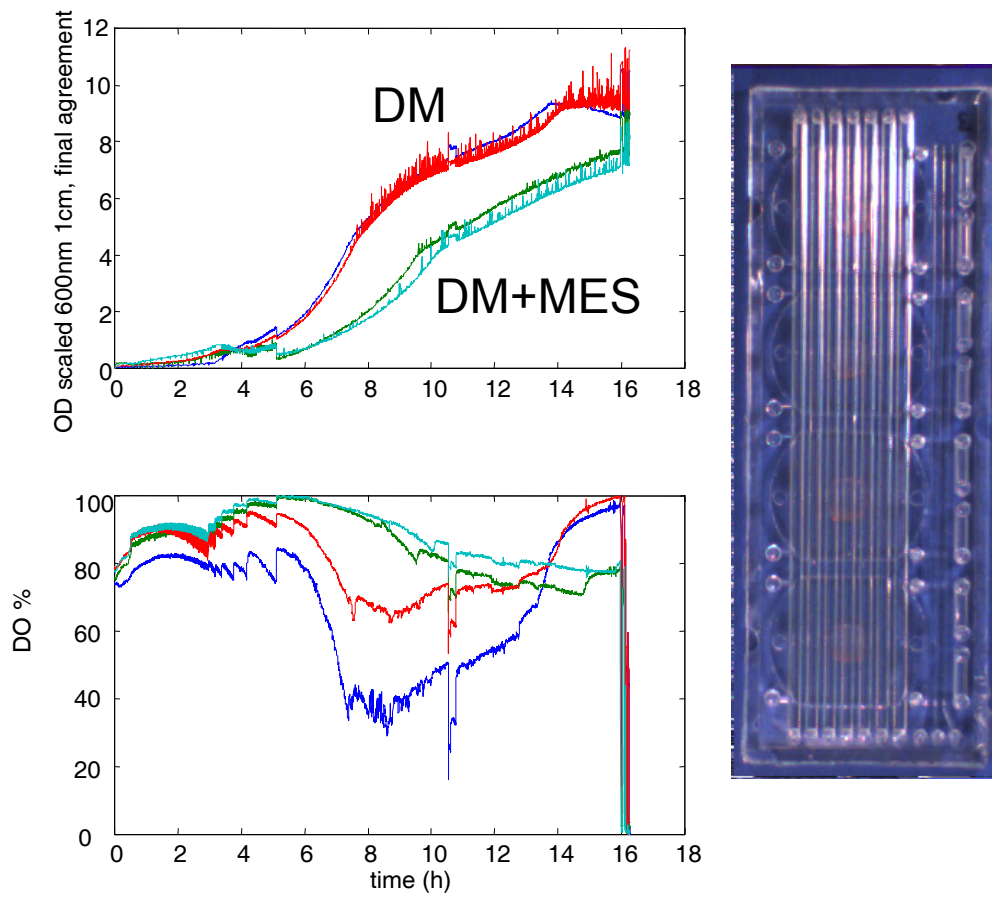


Fig. 21. Growth curves and dissolved oxygen curves for a phenylalanine producing *E. coli* strain (ATCC 31883) in defined medium with and without MES buffer. The photo on the right shows an example device with four growth wells and shared oxygenation and mixing tubes.